Hindawi
Advances in Civil Engineering
Volume 2022, Article ID 7174154, 9 pages
https://doi.org/10.1155/2022/7174154

Research Article

Experimental and Numerical Investigation of the Water-Exit Behaviour of an Inverted T-Shaped Beam

Xueyi Li[1] **and Feidong Zheng**[2]

[1]*College of River and Ocean Engineering, Chongqing Jiaotong University, Chongqing, China*
[2]*Power China Kunming Engineering Corporation Limited, Kunming, China*

Correspondence should be addressed to Feidong Zheng; feidongzheng@126.com

Received 20 July 2022; Revised 20 September 2022; Accepted 23 September 2022; Published 7 October 2022

Academic Editor: Jian Lin Liu

Water-exit is a hydraulic phenomenon induced when an object exists in a body of water. In the case of ship lifts, the hydrodynamic forces induced by the water-exit of the chamber's support beam may result in unsafe and unstable operating conditions and may even cause a loss of structural integrity. In this study, the water-exit process of a simplified beam was investigated using an experimental–numerical approach. The experimental results revealed that three major stages occur during water-exit: start-up, flow-around, and exit-moment. Moreover, the maximum additional hydrodynamic load exerted on the beam during water-exit occurred in the exit-moment phase. Based on these results, a calibrated numerical method was employed to analyse the main factors affecting the maximum additional hydrodynamic load. The numerical results indicated that the additional load can be accurately predicted using two dimensionless parameters. These results may help evaluate the negative impacts of suction on a ship lift chamber and improve the technical support and operation of ship lifts.

1. Introduction

Water-exit is a common phenomenon; for example, a water-exit response is induced when a fish jumps out of water [1], in submarines fire missiles [2], and while operating a marine crane. A launching type ship lift is a type of ship lift in which the ship lift's chamber is docked downstream in the water in order to cope with the large variation of the downstream water level. The launching ship lift of the Goupitan dam, located in the Guizhou province of China, is shown in Figure 1. To reduce the additional hydrodynamic load induced in the process of entering and exiting the water, the bottom plate of the chamber is usually designed as a wedge-shaped body, reinforced by a large number of longitudinal and transverse beams. Therefore, the safety of the ship lift is strongly dependent on the bearing capacity of the beams. When the ship lift chamber exits the water, the interaction between the bottom of the beams and the water produces a large negative pressure, resulting in additional tension on the lift's cables. Thus, the maximum negative pressure induced during water-exit must be considered in the design of the cables. However, once the beam has exited the water, the negative pressure rapidly resolves, resulting in severe vibrations on the ship lift chamber that may affect its safety and stability. Therefore, it is necessary to accurately evaluate the hydrodynamic load during water-exit.

Numerous studies have been conducted on water-exit problems. Greenhow [3] provided significant insight into the water-exit of a circular cylinder with both forced and free vertical motions using a CIP-based finite difference method. Later, Greenhow and Moyo [4] simulated the water-exit of a 2D horizontal circular cylinder using the boundary-element method (BEM) with a fully nonlinear free-surface boundary condition. They compared their calculated results with the small-time solution obtained by Tyvand and Miloh [5], at the initial stage of body motion, and a good agreement was achieved. Liju et al. [6] investigated the surge effects induced by cylindrical bodies. Korobkin [7] solved the water-exit problem via a linearised form of the mixed boundary value problem and by enforcing a Kutta-type condition at the

(a) (b) (c)

Figure 1: Launching ship lift at Goupitan dam. (a) The ship lift docks with the downstream. (b) Ship enters the ship lift. (c) The ship lift is out of the water.

contact point during the exit stage. This model was extended by Korobkin et al. [8] to include body motions, with time-dependent acceleration, and the water-exit response of a body whose shape changes over time. Rajavaheinthan and Greenhow [9] numerically investigated the forced constant acceleration exit of two-dimensional bodies through a free surface. To date, constant velocity water-exit problems have received less attention than water-exit problems with acceleration. However, during the water-exit process of a launching ship lift, T-shaped beams exit the water at a constant velocity, after a short initial acceleration. Thus, the mechanisms governing this water-exit problem are not fully understood and the identification and quantification of these aspects are essential.

In this study, a physical water-exit model was established to investigate the mechanism governing the water-exit of a ship lift chamber's support beam at a constant velocity. The hydrodynamic loads and flow patterns of the water were measured. Based on the experimental results, numerical modelling was further conducted to quantify the influence of relevant parameters on the characteristic load exerted on a beam during constant velocity water-exit. The findings could provide guidance for the design and operation of ship lifts.

2. Physical Model

2.1. Experimental Set-Up and Experiments. An inverted T-shaped beam is commonly used in ship lift chambers with a length-to-width ratio >10. In this context, the beam's water-exit can be simplified to a two-dimensional problem. In this study, the beam was modelled by referring to the Goupitan ship lift. The model was constructed using polyvinyl chloride (PVC) and comprised a 0.01 m thick web and flange. The model was 0.9 m long, 0.4 m wide, and 0.5 m high. A water tank was used to provide a 0.5 m deep initially still water region. The tank was 1 m long and wide and had a total depth of 0.7 m. The tank was made of plexiglass to enable visual observation of the water-exit process. A hydraulic hoist fixed to a steel structure was used to raise and lower the beam model. A guide rail was used to keep the flange parallel to the still water surface during the water-exit process. A schematic and a photograph of the experimental set-up are shown in Figures 2 and 3, respectively.

The hydrodynamic pressure beneath the flange was measured using five pressure sensors, with an accuracy of 10 Pa. The sensors had a round head with a diameter of 5 mm. The five sensors were arranged as shown in Figure 4, spaced at 40 mm. The first sensor, $P1$, was located 22 mm from the centre of the web, and an ultrasonic displacement sensor, fixed to the steel structure, was used to record the vertical displacement of the flange. The ultrasonic displacement sensor can measure movement in a 0 to 1 m range with an accuracy of ±0.1%. Data from the pressure and ultrasonic displacement sensors were collected by the Donghua acquisition system at a sampling frequency of 500 Hz, as shown in Figure 5. The water-exit process was recorded using a 1 MP high-speed camera operating at 100 fps. During the experiment, the flange was initially located 0.175 m below the calm water surface.

2.2. Basic Features

2.2.1. Pressure Evolution During Water-Exit. The velocity, v, and displacement, S, of the beam during the water-exit process are shown in Figure 6. The displacement was obtained by direct measurement of the model, and the velocity was subsequently determined as the derivative of S, with regard to time. The beam started to move at $t = 1$ s and accelerated to 0.041 m/s with a constant acceleration of 0.12 m/s^2 and then maintained a relatively constant velocity. At $t = 5.5$ s, the bottom of the beam was removed from water.

Figure 7 shows the temporal evolution of the dynamic pressure beneath the beam during the water-exit process. A 350 Pa pressure change occurred immediately after when the beam began to move (1 s). Subsequently, the pressure value decreased as the beam was lifted out of the water. Each

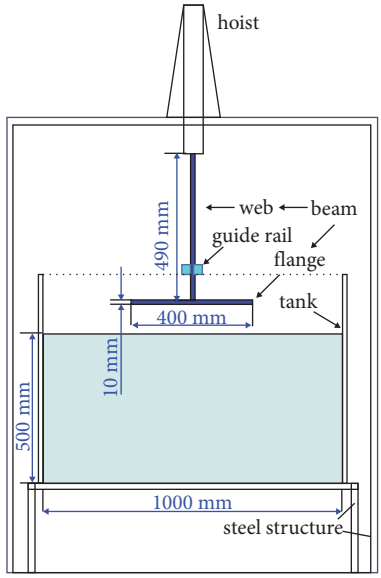

Figure 2: Model device diagram.

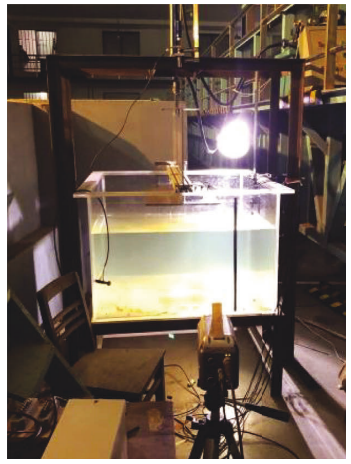

Figure 3: Model photo.

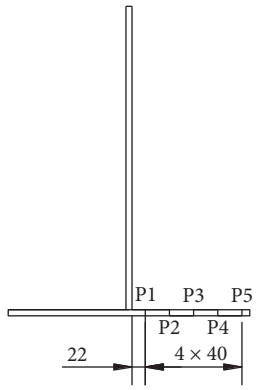

Figure 4: Pressure sensor arrangement.

pressure sensor experienced a negative pressure when the bottom of the beam was pulled beyond the water surface. The maximum negative pressure was −280 Pa.

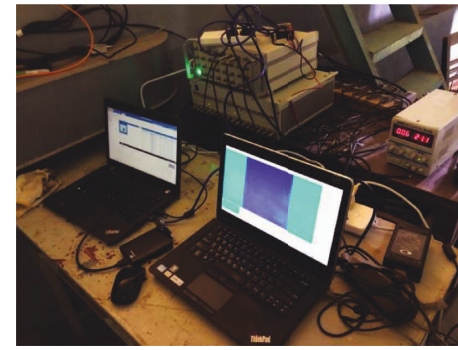

Figure 5: Acquisition devices.

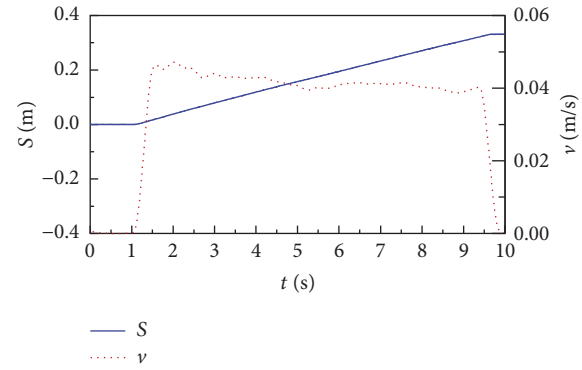

Figure 6: Displacement and velocity of the beam.

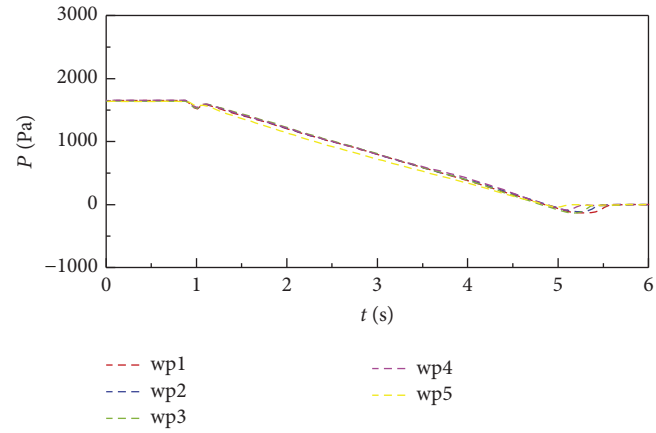

Figure 7: Evolution of the dynamic pressure beneath the beam.

2.2.2. Flow Patterns Evolution During Water-Exit. Different patterns were observed during the water-exit process of the beam. In this section, the water-exit process has been categorised into three major stages based on the pressure measurements and visual observations.

The first stage is the start-up acceleration stage, as shown in Figure 8. During this stage, no dramatic change in the flow pattern could be observed; however, a sudden change in the hydrodynamic load beneath the flange was recorded.

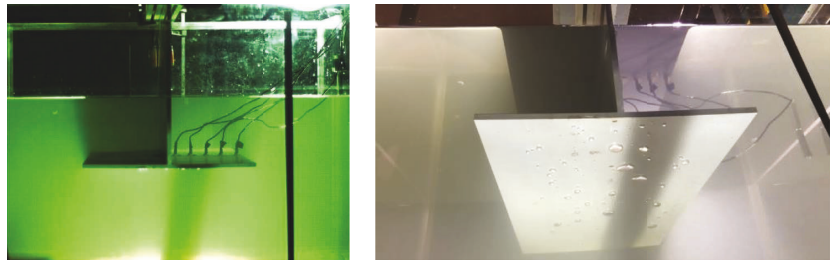

(a) (b)

Figure 8: Flow pattern of the initial acceleration stage.

The second stage was the flow resistance stage, in which drag induced an additional hydrodynamic load on the beam. During this stage, a noticeable bulge at the water surface was observed; however, the top of the moving flange was still submerged in the water, as shown in Figure 9.

The third phase was defined as the suction stage, where an additional hydrodynamic load was exerted on the beam due to suction. This stage begins when the top of the flange reaches the average surface level in the tank. The water above the flange first flowed towards the edges of the flange owing to gravity. Subsequently, a concave water body was created above either side of the flange and ripples formed along its edges, as shown in Figures 10(a)–10(f). A thin water layer was attached to the bottom of the flange when its level was slightly higher than the average water surface level due to molecular adsorption of water. As the flange rose out of the water, the adsorption layer began to separate from the water body in the tank, with a consistent decrease in the contact area between them, as shown in Figures 10(g)–10(l). It was also observed that the water droplets beneath the flange flowed towards its centre owing to the influence of air flow around the flange and air supply on both its edges.

3. Numerical Simulation

3.1. Computational Domain and Boundary Conditions. Numerical modelling of the water-exit process was performed based on the conditions of the physical experiment. The two-dimensional numerical model was developed in the vertical plane with the same layout and size as the physical model. The computational domain was bounded by the beam, tank sidewalls, tank bottom, and upper boundary. The wall boundary condition was imposed on the beam, tank sidewalls, and the bottom of the tank. A pressure outlet condition was imposed on the upper boundary. The computational domain was discretized by structured meshes in the flange zone (mesh size of 0.5 mm). The computational domain and simulation mesh are shown in Figure 11.

The dynamic mesh method was used to simulate the relative motion between the beam and tank, and the layering method was used to update the mesh. To simulate the motion of the flange, the bottom of the tank was set as the moving zone, which moved downwards at a velocity equal to the physical beam's speed. The tank sidewalls were set as the deformation zones, where mesh splitting and deformation occurred, and the fluid was modelled using the Reynolds-averaged Navier–Stokes equations in their incompressible two-phase form. The turbulence was modelled using the renormalisation group k-ε turbulence model. The interface between water and air was tracked by the volume of the fluid model, assuming densities of 998.2 kg m^{-3} and 1.225 kg m^{-3}, respectively. An explicit scheme was applied for time discretisation, whereas the second-order upwind scheme was used for spatial discretisation. In addition, the SIMPLE algorithm was used for the velocity and pressure coupling.

3.2. Validation and Verification. Figure 12 compares the temporal evolution of the simulated water surface during the water-exit process to that of the experimental observations. Excellent agreement between the numerical and experimental results was observed. The various flow phenomena involving the water surface bulge, liquid surface suction, liquid surface shrinkage, and water droplet formation and movement were reproduced by the numerical model.

The temporal evolution of the pressure beneath the flange obtained from both the experimental results and numerical model is shown in Figure 13, wherein the numerical trends agreed with the experimental results. However, as the flange exited the water, an enclosed air pocket was formed in the numerical simulations, whereas in the physical experiments, the water curtain was discontinuous; thus, no air pocket could form and the pressures in the region were atmospheric. This led to the numerical model including an additional negative pressure while lifting the beam, shown as pressure spikes in Figure 13. Nevertheless, the maximum suction pressure occurred before the formation of the water curtain; thus, the deviation of the simulated pressures from the measured results could be neglected in terms of the maximum suction pressure prediction.

Overall, a reasonable agreement between the experimental and numerical solutions was achieved, and the computed maximum negative pressures were close to the measured values with an error of less than 10%.

3.3. Simulation Conditions. The suction force exerted on the beam during water-exit was governed by two relevant parameters: flange width, b, and exit velocity, v. Initially, the still water depth in the tank was 1.2 m with a corresponding

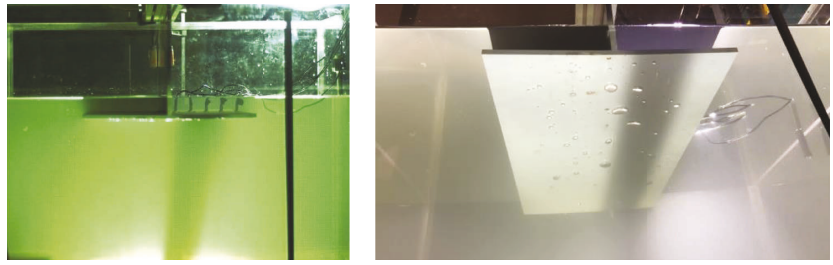

(a) (b)

Figure 9: Flow pattern of the flow resistance stage.

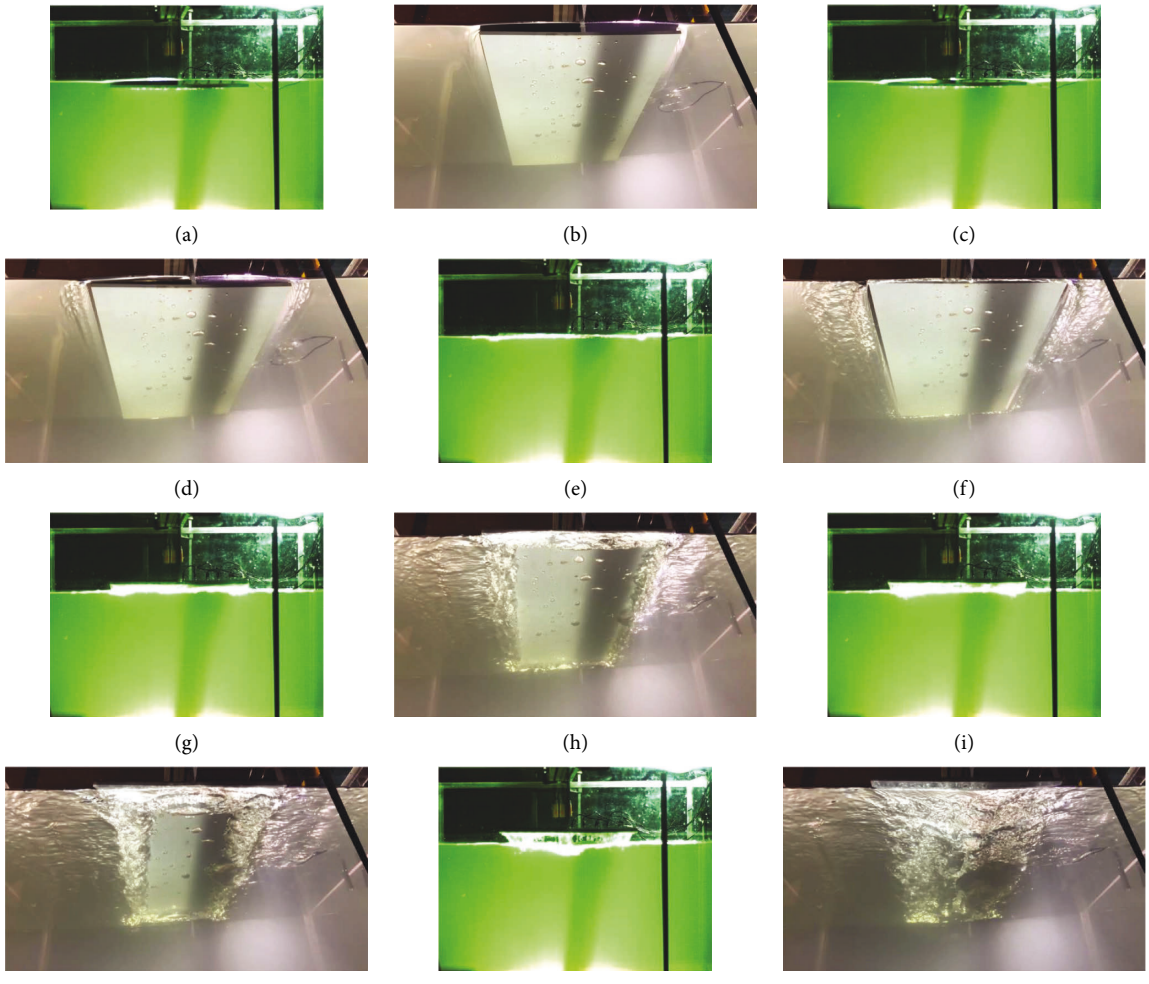

(a) (b) (c)

(d) (e) (f)

(g) (h) (i)

(j) (k) (l)

Figure 10: Flow pattern of the suction stage.

water level of $y = 0.4$ m, whereas the bottom of the flange was at $y = 0$ m. The flange moved through a travel distance of 0.5 m at a constant velocity, with an initial acceleration of 0.1 m/s^2. Overall, 25 simulations were conducted using five flange widths of 0.2, 0.4, 0.6, 0.8, and 1.0 m and five different exit velocities in the range 0.017–0.2 m/s.

3.4. Data Analysis

3.4.1. Total Hydrodynamic Load. The variation of the total hydrodynamic load during the water-exit process is shown in Figure 14, for $b = 0.4$ m and $v = 0.034$ m/s. Two distinct stages can be observed during the travelling process of the

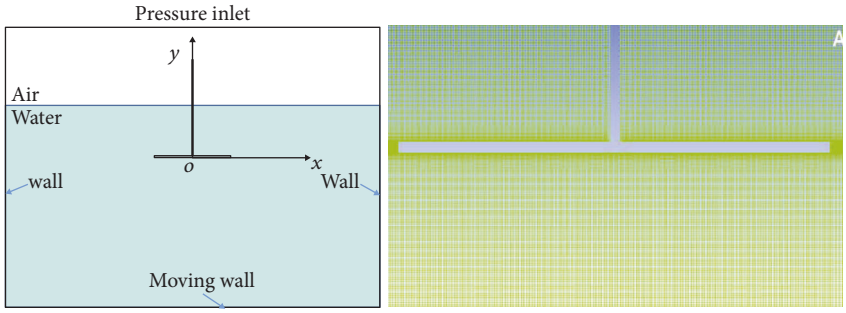

Figure 11: Computational domain and simulation mesh.

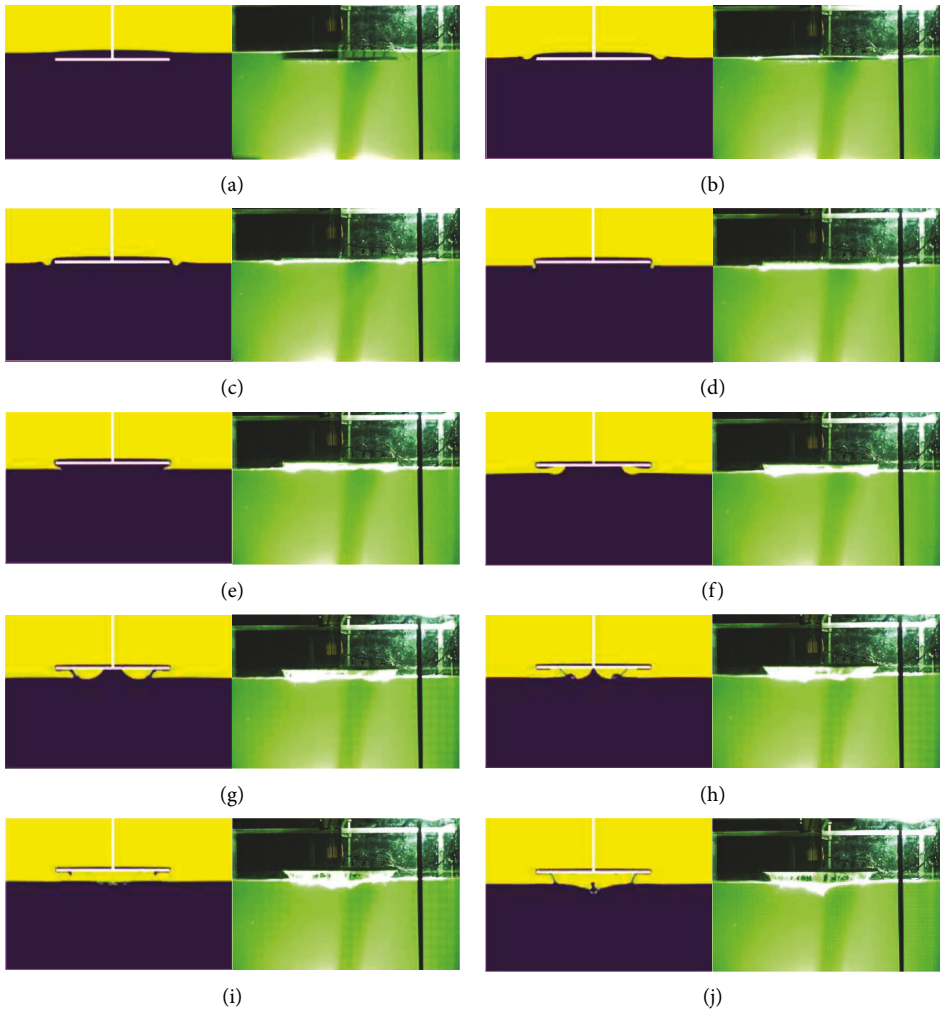

Figure 12: Comparison between the computed and experimental water-exit processes. (a) $t = 5.28$ s. (b) $t = 5.32$ s. (c) $t = 5.35$ s. (d) $t = 5.37$ s. (e) $t = 5.39$ s. (f) $t = 5.40$ s. (g) $t = 5.41$ s. (h) $t = 5.42$ s. (i) $t = 5.43$ s. (j) $t = 5.44$ s.

beam: a constant acceleration stage and a constant velocity stage. In the first stage, the hydrodynamic load decreased until a value of 75 N/m. In the second stage, the load initially increased followed by a gradually decreasing trend until the top of the beam reached the average water surface. Then, a sharp drop in the load was observed, and the corresponding maximum load was approximately −80 N/m.

3.4.2. Virtual Buoyancy. In this study, virtual buoyancy was defined as the buoyancy exerted on the beam, assuming the water in the tank was quiet at a given time in the entire water-exit process. In Figure 15, the virtual buoyancy variation corresponding to a test with $b = 0.4$ m and $v = 0.034$ m/s is presented. Overall, the virtual buoyancy exhibited a monochromatic descending trend before the beam was lifted

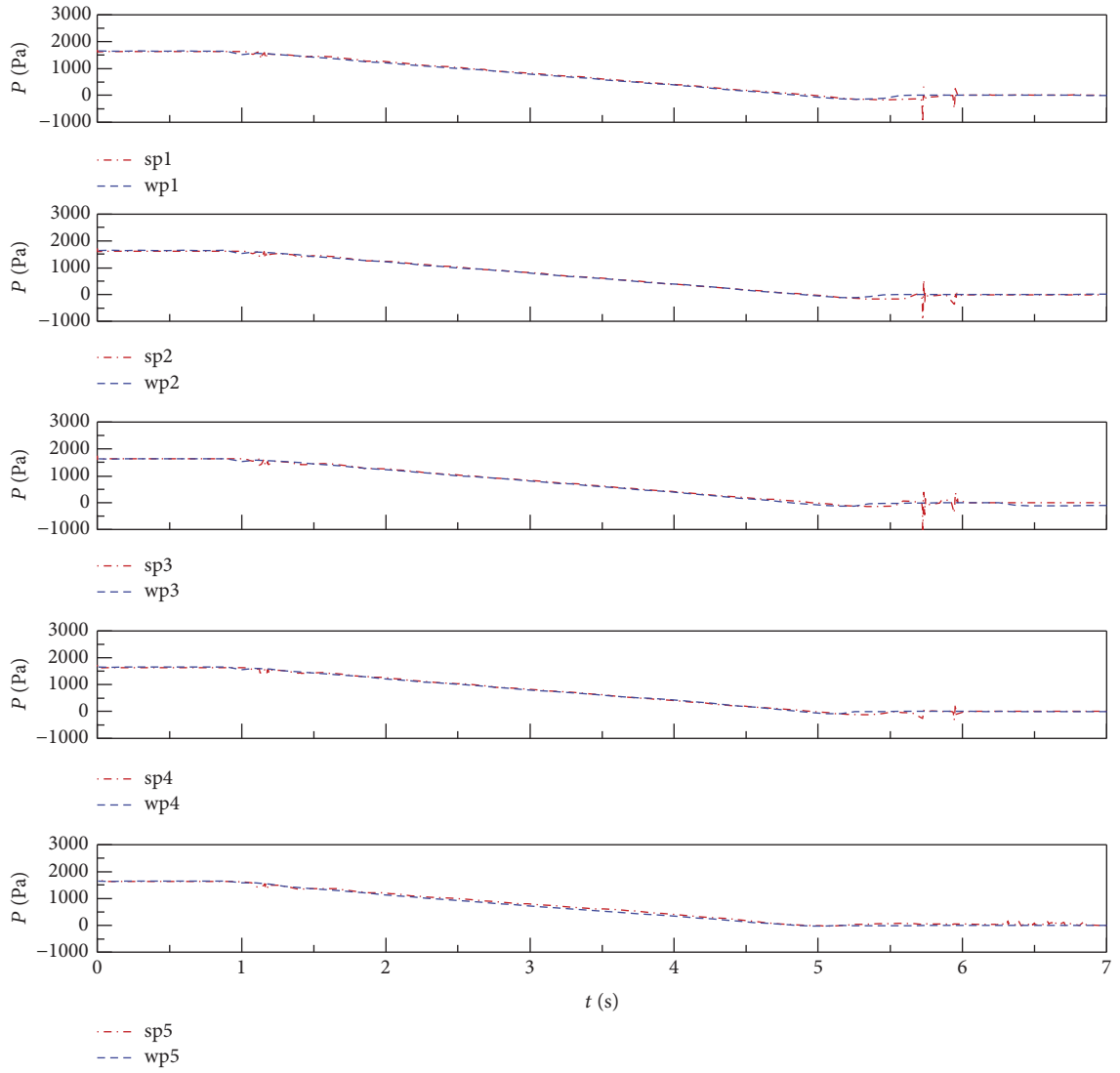

Figure 13: Comparison of computed and measured dynamic pressure.

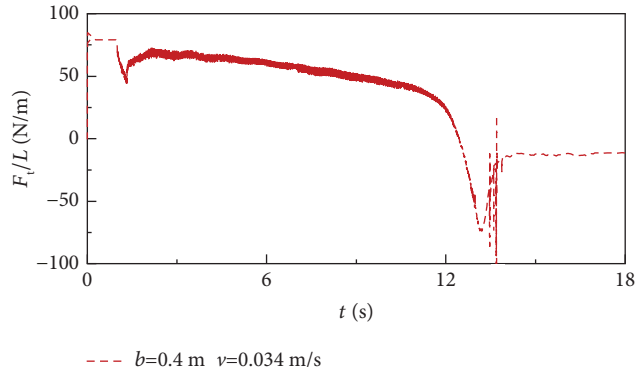

Figure 14: Total hydrodynamic load evolution during the water-exit process.

out of the water body. It should be noted that the decrease in the virtual buoyancy was due to the reduction of the submerged depth above the beam top, whereas it was attributed to the decrease in the beam volume surrounded by water.

3.4.3. Additional Hydrodynamic Loads. The additional hydrodynamic load is defined as the difference between the total hydrodynamic load and the virtual buoyancy. Figure 16 presents the additional hydrodynamic load during the

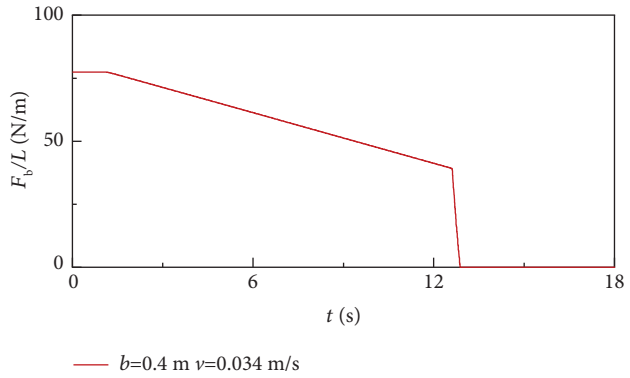

Figure 15: Virtual buoyancy evolution during the water-exit process.

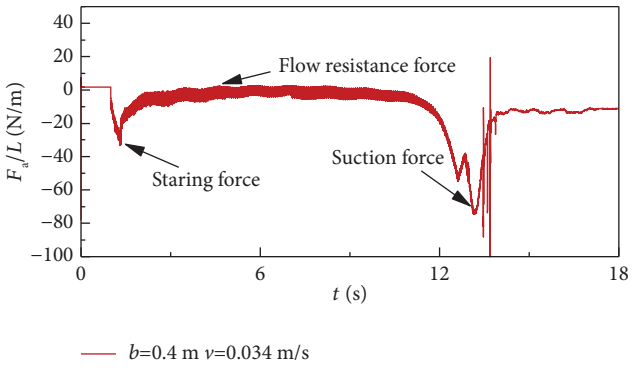

Figure 16: Additional hydrodynamic load evolution during the water-exit process.

water-exit process. In the acceleration stage, the additional hydrodynamic load decreased and reached the first minimum of 35 N/m. Then, the load increased rapidly and then remained constant during the constant velocity stage. The load reached its second minimum value of −80 N/m shortly before the fluid separation of the suctioned water beneath the beam and the water in the tank. This load is of key interest in facility protection and is defined as the suction load.

3.4.4. Prediction of the Suction Load. Hydraulic considerations have demonstrated that the suction load per unit length, F_s/L, depends mainly on the following variables [10]:

$$\frac{F_s}{L} = f(v, b, \rho, g, \mu), \tag{1}$$

where ρ is the water density, g is the acceleration due to gravity, and μ is the dynamic viscosity of the water. Dimensional analysis leads to the following mathematical expression:

$$\frac{F_s}{1/2\rho v^2 bL} = f\left(\frac{gb}{v^2}, \frac{\mu}{\rho v b}\right). \tag{2}$$

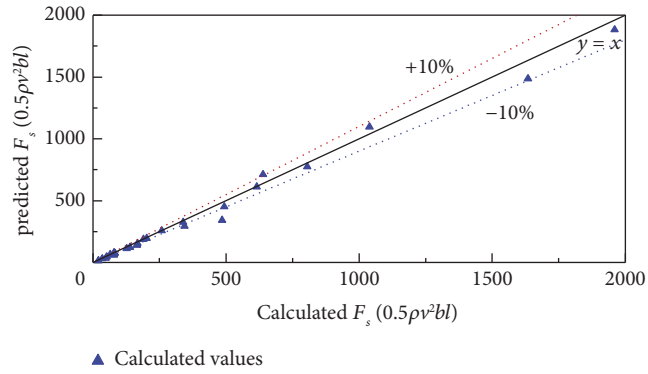

Figure 17: Calculated versus predicted normalized suction loads.

Multiple regression for the normalized suction load, $F_s/(1/2\rho v^2 bL)$, yields

$$\frac{F_s}{1/2\rho v^2 bL} = 0.036\left(\frac{gb}{v^2}\right)^{0.78}\left(\frac{\mu}{\rho v b}\right)^{-0.28}. \tag{3}$$

With a correlation coefficient of $r2 = 0.99$, a comparison of the $F_s/(1/2\rho v^2 bL)$ values predicted using equation (3) and the calculated values are illustrated in Figure 17. The results were in close agreement with the line of perfect agreement and the maximum relative deviation from the calculated values was approximately 10%.

4. Conclusions

In the case of ship lifts, the hydrodynamic forces induced during water-exit of the chamber's beam may result in unsafe and unstable operating conditions. In this study, a physical model of a simplified beam was constructed to investigate the basic flow patterns developed during the water-exit process. Based on the experimental results, numerical modelling was performed to analyse the factors that govern the water-exit process. The main findings of this study are summarised as follows:

(1) The exit-water process can be categorised into three major stages, namely, the start-up phase, flow-around phase, and suction phase. The maximum additional hydrodynamic load occurred during the suction phase and should be considered during the design and operation of ship lifts.

(2) Based on dimensional analysis and the results of numerical simulation, an empirical equation was derived to express the normalized maximum suction load in terms of two dimensionless parameters. This enables a direct evaluation of the expected maximum suction load during the water-exit process.

These results may help evaluate the negative impacts of suction forces on ship lift chambers and improve the technical support for ship lift operation.

Data Availability

The data used to support the findings of this study are available from the corresponding author upon request.

Conflicts of Interest

The authors declare that there are no conflicts of interest regarding the publication of this article.

Acknowledgments

The administrative support of Yaan Hu should be acknowledged. This study was supported by the China Postdoctoral Fund (Grant No. 2021M700620); Natural Science Foundation of Chongqing, China (Grant No. cstc2020jcyj-bshX0043; cstc2021jcyj-bshX0049).

References

[1] A. Khosronejad, L. Mendelson, A. H. Techet, D. Angelidis, and F. Sotiropoulos, "Water exit dynamics of jumping archer fish: integrating two-phase flow large-eddy simulation with experimental measurements," *Physics of Fluids*, vol. 32, no. 1, Article ID 011904, 2020.

[2] Y. Wang, L. Liao, T. Du et al., "A study on the collapse of cavitation bubbles surrounding the underwater-launched projectile and its fluid–structure coupling effects," *Ocean Engineering*, vol. 84, pp. 228–236, 2014.

[3] M. Greenhow, "Water-entry and-exit of a horizontal circular cylinder," *Applied Ocean Research*, vol. 10, no. 4, pp. 191–198, 1988.

[4] M. Greenhow and S. Moyo, "Water entry and exit of horizontal circular cylinders," *Philosophical Transactions of the Royal Society of London,Series A: Mathematical, Physical and Engineering Sciences*, vol. 355, pp. 551–563, 1997.

[5] P. A. Tyvand and T. Miloh, "Free-surface flow due to impulsive motion of a submerged circular cylinder," *Journal of Fluid Mechanics*, vol. 286, pp. 67–101, 1995.

[6] P. Y. Liju, R. Machane, and A. Cartellier, "Surge effect during the water exit of an axisymmetric body traveling normal to a plane interface: experiments and BEM simulation," *Experiments in Fluids*, vol. 31, no. 3, pp. 241–248, 2001.

[7] A. A. Korobkin, "A linearized model of water exit," *Journal of Fluid Mechanics*, vol. 737, pp. 368–386, 2013.

[8] A. A. Korobkin, T. I. Khabakhpasheva, and K. J. Maki, "Hydrodynamic forces in water exit problems," *Journal of Fluids and Structures*, vol. 69, pp. 16–33, 2017.

[9] R. Rajavaheinthan and M. Greenhow, "Constant acceleration exit of two-dimensional free-surface-piercing bodies," *Applied Ocean Research*, vol. 50, pp. 30–46, 2015.

[10] H. Chanson, *The Hydraulics of Open Channel Flows: An Introduction*, Butterworth-Heinemann, Oxford, UK, 2004.